# Wear detection for progressing cavity pumps with system identification methods

**J. Müller** * **Y. Kouhi** * **S. Leonow** * **M. Mönnigmann** *

* *Automatic Control and Systems Theory, Ruhr-Universität Bochum, Universitätsstraße 150, 44801 Bochum, Germany (e-mail: {jens.mueller-r55, yashar.kouhi, sebastian.leonow, martin.moennigmann}@rub.de).*

**Abstract:** We present a model-based approach for a non-invasive online wear detection for progressing cavity pumps. The approach is based on a model of the rotor displacement. All unknown model parameters can be determined from measured data with a recursive-least-squares algorithm, which can efficiently be run on an embedded device. The identified model parameters provide information about the internal wear. Without the model-based approach, wear can only be analysed after disassembling the pump. We evaluate the proposed approach in a laboratory test setup with an undersize rotor, which simulates a worn pump. The results show the proposed approach can reliably monitor wear.

*Keywords:* predictive maintenance, fault detection, parameter estimation, positive displacement pumps

## 1. INTRODUCTION

Wear detection and the prediction of the remaining service life are crucial steps in industrial asset management. Many hardware sensors and soft sensors for wear detection in rotating machinery have been developed. This holds in particular for fundamental components like pumps and compressors (see, e.g., Mohanty et al. (2012)).

Wear dynamics are well-understood for centrifugal pumps. Other pump types, in contrast, have not been addressed and sensors for measuring their wear are not available. This holds for progressing cavity pumps (PCPs) in particular. Because PCPs often transport fluids with high viscosity or a high solid fraction, conventional sensors like inductive flow meters can often not be used. In fact, PCPs are usually shut down and disassembled to allow visual checks for wear of rotors and stators. This is surprising, since PCPs are often installed in applications with high demands on availability, such as environmental engineering, sewage treatment and sewage disposal (Nelik and Brennan, 2005, pp. 105). A wear detection method that does not require the PCP to be disassembled is of obvious interest.

Under ideal conditions, the flow rate through the PCP is proportional to the rotational speed and independent of the differential pressure across the pump. In real applications, an increased differential pressure leads to a certain back flow due to imperfect sealings between rotor and stator. Increased back flow reduces the efficiency of the pump. As the wear of rotor and stator increases, the shape of the sealings, formed by the rotor-stator contact, changes and the back flow increases.

PCP malfunction and the responsible wear mechanisms have been studied before (see, e.g., Wirth (1993), Delpassand (1997) and Liang et al. (2011)). All existing approaches require data from a disassembled pump, however. We introduce a method for wear detection that does not require the PCP to be disassembled. We derive a model of the rotor displacement inside the stator and show all model parameters can be estimated online with a recursive-least-squares algorithm. Because wear essentially affects the parameters that govern the rotor dynamics, wear can be monitored by monitoring the estimated model parameters.

Section 2 summarizes facts about PCPs as needed for the paper. The rotor displacement model is summarized in Section 2.1 and used to derive a simple wear detection model in Section 2.2. Section 2.3 treats the parameter estimation problem. Section 3 introduces the laboratory setup used for the validation of the method. Results are presented and discussed in Section 4. A brief conclusion is given in Section 5.

## 2. DYNAMIC MODEL AND ONLINE PARAMETER ESTIMATION

We consider single-stage, single lobe progressing cavity pumps driven by electric motors. Figure 1 shows a sketch and introduces some basic terminology. The geometries
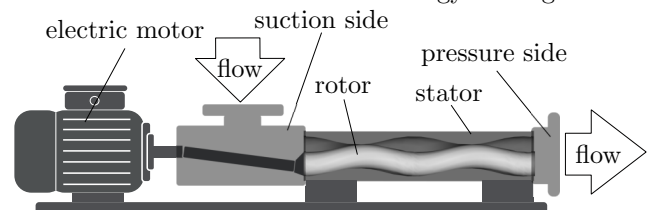


Fig. 1. Pump unit with electric motor.

of the rotor and stator force the rotor to perform two superposed movements: it rotates around its central axis $C_A$ with the speed $\dot{\psi}$, where $\psi$ is the rotational angle of the

rotor. Due to the eccentricity of the rotor, the central axis $C_A$ simultaneously moves on a closed curve. This rotation occurs with the same speed, but in the direction opposite to the rotation in $\psi$. We refer to the rotational angle of the second motion by $\varphi$. Assuming ideal geometries and no disturbances, the closed curve parametrized by $\varphi$ is a circle. We refer to the closed curve, depicted by the dashed
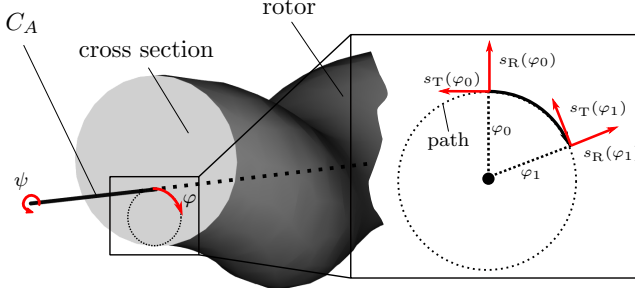


Fig. 2. Left: superposed movements of the rotor with corresponding angles for ideal geometries and no disturbances. Right: directions of the deviations from a reference path for two different rotational angles $\varphi_0$ and $\varphi_1$.

line in Figure 2, as the *path* of the rotor. The center point of the path lies on the center axis of the stator geometry under ideal conditions.

The path deviates from the ideal circle due to deviations of the real rotor and real stator geometries from the ideal ones. The real path is also a function of the differential pressure, the rotational speed $\dot{\psi}$ and the temperature of the stator, where the influence of the differential pressure is the strongest one (Müller, 2017). We assume that the actual path of the rotor can be measured once, i.e., for the new pump. We treat deviations of the path from this reference path from hereon.

### 2.1 Rotor displacement model

Müller et al. (2019) proposed a rotor-stator model that describes, based on force and mass balances, the deviation from a reference path as a function of the differential pressure. We summarize those aspects of the model that are required for the present paper.

The model can conveniently be stated in a coordinate system that is fixed with respect to the rotor. The orientation of the coordinate system is therefore a function of $\varphi$. See Figure 2 for an illustration for two sample angles, $\varphi_0$ and $\varphi_1$. The displacement of the rotor from its reference path is divided into two components, the tangential deviation $s_T(\varphi)$ and the radial deviation $s_R(\varphi)$. Only the tangential deviations are required in the present paper. Let $s_{s,T}(\varphi)$ and $s_{p,T}(\varphi)$ refer to the tangential deviation on the suction and pressure side of the pump, respectively.

The contact between rotor and stator can be modeled with three spring-damper-systems defined by the spring coefficients $c_1$, $c_2$ and $c_3$ and the damping factors $d_1$, $d_2$ and $d_3$. The rotor is modeled as a straight beam with the parameters length $l_R$, mass $m$, inertia $J$ and center of gravity $C$. Note that the exact geometry of the rotor is not required to be known. Figure 3 illustrates the rotor-stator model.
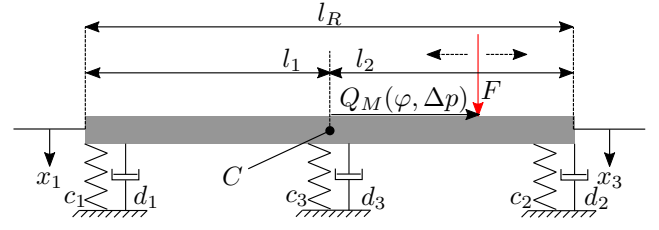


Fig. 3. Rotor-stator model (suction side left, pressure side right)

The model for the tangential deviation of the rotor from the reference path reads

$$\dot{x}_1 = x_2 \tag{1}$$

$$\begin{aligned}
\dot{x}_2 = -\frac{1}{2Jm}\Big[&(2Jc_1 + Jc_3 + 2ml_1^2c_1)x_1 \\
&+ (2Jd_1 + Jd_3 + 2ml_1^2d_1)x_2 \\
&+ (2Jc_2 + Jc_3 - 2ml_1l_2c_2)x_3 \\
&+ (2Jd_2 + Jd_3 - 2ml_1l_2d_2)x_4\Big] \\
&- \frac{2ml_1Q_M(\varphi,\Delta p) - 2J}{2Jm}F
\end{aligned} \tag{2}$$

$$\dot{x}_3 = x_4 \tag{3}$$

$$\begin{aligned}
\dot{x}_4 = -\frac{1}{2Jm}\Big[&(2Jc_1 + Jc_3 - 2ml_1l_2c_1)x_1 \\
&+ (2Jd_1 + Jd_3 - 2ml_1l_2d_1)x_2 \\
&+ (2Jc_2 + Jc_3 + 2ml_2^2c_2)x_3 \\
&+ (2Jd_2 + Jd_3 + 2ml_2^2d_2)x_4\Big] \\
&+ \frac{2ml_2Q_M(\varphi,\Delta p) + 2J}{2Jm}F,
\end{aligned} \tag{4}$$

where $x_1 = s_{s,T}$, $x_2 = \dot{s}_{s,T}$, $x_3 = s_{p,T}$, $x_4 = \dot{s}_{p,T}$ and $l_1$, $l_2$ are as in Figure 3. $F$ is the magnitude of the force on the rotor that results from the differential pressure. The force acts parallel to the direction of $x_1$ at a distance $Q_M(\varphi,\Delta p)$ from the center of gravity $C$ (see Figure 3), where

$$Q_M(\varphi,\Delta p) = \frac{l_R}{2} - \frac{3}{4}P_S + \frac{P_S}{2\pi}\cdot\text{mod}(\varphi - \gamma(\Delta p), \pi), \tag{5}$$

with the stator pitch $P_S$. The model parameters $l_R$, $P_S$, $J$, $m$, $l_1$ and $l_2$ can be obtained from the data sheet provided by the pump manufacturer. The parameters $c_i$ and $d_i$, in contrast, are unknown and need to be estimated (see Section 2.3).

Equation (5) implies $Q_M(\varphi,\Delta p)$ is a discontinuous function of $\varphi$ and $\Delta p$. The discontinuity in (5) occurs at $\varphi = \gamma(\Delta p) + k\pi$, $k \in \mathbb{N}$, where $\gamma(\Delta p)$ depends on the mounting angle of the stator and the differential pressure. The angle $\gamma(\Delta p)$ can be described by

$$\gamma(\Delta p) = \gamma_0 - \gamma_1\Delta p, \tag{6}$$

where $\gamma_0$ is the mounting angle of the stator and $\gamma_1$ models the dependence on the differential pressure $\Delta p$. Both coefficients, $\gamma_0$ and $\gamma_1$, only have to be determined once after the installation of the stator (see Section 3). We refer to $\gamma(\Delta p)$, as the *angular offset*.

We refer to Müller et al. (2019) for additional information on the rotor displacement model.

## 2.2 Model simplifications for wear detection

The rotor performs a tilting motion during the operation of the pump. The degree of wear can be monitored by monitoring this tilting motion. The ability to tilt is characterized by the spring and damping constants $c_1$, $d_1$ on the suction side and $c_2$ and $d_2$ on the pressure side. The spring and damping constants $c_3$ and $d_3$ are located in the middle of the rotor (close to $C$) and thus have a negligible effect on the tilting motion.

Because the effect of $c_3$ and $d_3$ is negligible, a model that only depends on $c_1$, $d_1$, $c_2$ and $d_2$ suffices. Subtracting (4) from (2) and dividing by $(l_1 + l_2)$ yields a suitable model equation. It reads

$$\frac{J(\dot{x}_4 - \dot{x}_2)}{(l_1 + l_2)} - Q_M(\varphi, \Delta p)F$$
$$= l_1 x_1 c_1 - l_2 x_3 c_2 + l_1 x_2 d_1 - l_2 x_4 d_2 \,.$$

If we furthermore assume $C$ to be located in the center of the rotor, i.e., $l_1 = l_2 = l$, this equation becomes

$$\frac{J(\dot{x}_4 - \dot{x}_2)}{2l^2} - \frac{Q_M(\varphi, \Delta p)}{l}F \qquad (7)$$
$$= x_1 c_1 - x_3 c_2 + x_2 d_1 - x_4 d_2 \,.$$

The tangential deviations $s_{\mathrm{s,T}} = x_1$ and $s_{\mathrm{p,T}} = x_3$ can be determined with inductive distance sensors. Their derivatives $x_2 = \dot{s}_{\mathrm{s,T}}$, $x_4 = \dot{s}_{\mathrm{p,T}}$ and $\dot{x}_2$, $\dot{x}_4$ can reliably be approximated with finite differences with an accuracy that is sufficient for the present approach. When substituting values for $x_1, \ldots, x_4$, $\dot{x}_2$ and $\dot{x}_4$, (7) becomes an algebraic equation. The unknown parameters $c_1$, $d_1$, $c_2$ and $d_2$ in this equation can be determined with a recursive-least-squares (RLS) estimation, which is detailed in the next section.

## 2.3 Online parameter estimation

We assume the tangential deviations $x_1 = s_{\mathrm{s,T}}$ and $x_3 = s_{\mathrm{p,T}}$ and $\varphi$ can be determined at times $t = k T_s$, $k \in \mathbb{N}$ for some sampling time $T_s$. Furthermore, we assume the first order derivatives $x_2 = \dot{s}_{\mathrm{s,T}}$, $x_4 = \dot{s}_{\mathrm{p,T}}$ and second order derivatives $\dot{x}_2$, $\dot{x}_4$ can be approximated at time points $k$ with finite differences by choosing $T_s$ sufficiently small [1]. Let

$$z(k) = \frac{J(\dot{x}_4 - \dot{x}_2)}{2l^2} - \frac{Q_M(\varphi, \Delta p)}{l}F \,, \qquad (8a)$$

$$\xi(k) = [x_1 \quad -x_3 \quad x_2 \quad -x_4]^T \,, \qquad (8b)$$

where all values on the right hand sides are understood to be measured at time $k$, and let

$$\theta(k) = [c_1(k) \; c_2(k) \; d_1(k) \; d_2(k)]^T \qquad (8c)$$

be the time-variant vector containing the unknown parameters. Then (7) can be written as

$$z(k) = \theta^T \xi(k) \qquad (9)$$

as a preparation to the application of the RLS estimation.

The RLS estimation is based on the least-squares (LS) problem that minimizes the sum of the squared residuals of a measured signal $z(k)$ and a predicted signal $\hat{z}(k)$ for a certain period of time (see, e.g., Nguyen (2018, pp. 126)). LS estimations are typically used for offline parameter

---

[1] Finite difference approximations can only be calculated after some time points have elapsed. Let $k = 0$ refer to the first time point for which all finite differences can be calculated without restriction.

estimation with recorded data. For an online parameter estimation, it is more practical to use a recursive algorithm that updates the current best estimate whenever a new measurement becomes available. RLS estimation is particularly suitable for this purpose here due to the linear dependence of (7) on the parameters $c_i$ and $d_i$ (Åström and Wittenmark, 1989, pp. 42). The RLS estimation requires evaluating

$$W(k) = \frac{P(k-1)\xi(k)}{\lambda + \xi(k)^T P(k-1)\xi(k)},$$
$$\hat{\theta}(k) = \hat{\theta}(k-1) + W(k)\left(z(k) - \xi(k)^T \hat{\theta}(k-1)\right), \qquad (10)$$
$$P(k) = \left(I - W(k)\xi(k)^T\right) P(k-1)/\lambda,$$

in every time step $k$, where $P(k)$ and $W(k)$ are the measurement covariance matrices and the estimator gain matrices, respectively, at time point $k$. The parameter $0 \le \lambda \le 1$ is a forgetting factor that is used to weight the newer measured data more strongly (Åström and Wittenmark, 1989, pp. 52).

Figure 4 summarizes the inputs and parameters of the estimation algorithm and process. The rotational angle $\varphi$ and the differential pressure $\Delta p$ are measured directly. The tangential deviations $s_{\mathrm{s,T}}$, $s_{\mathrm{p,T}}$ are determined with distance transmitters (Müller et al., 2019). The angular offset (6) is described by $\gamma_0$ and $\gamma_1$, which enter the calculation of $z(k)$ and have to be determined once after the pump is assembled (Section 3). The RLS algorithm needs to be initialized with $\hat{\theta}(0)$, $\lambda$ and $P(0)$. Their numerical values are given in Section 4.
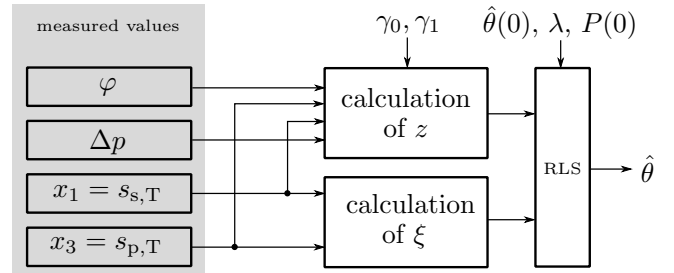
Fig. 4. Scheme of the estimation process.

# 3. LABORATORY TEST SETUP

We apply the proposed approach to the process sketched in Figure 5. Water is pumped from a container a) by the PCP c) and passes through a control valve b) before it returns into the container. Various points of operation can be established by adjusting the pump speed and the valve opening.

The distance transmitters (DT) are mounted centrically and equally distributed in the suction side and pressure side housing of the pump (see Figure 6). Eight distance transmitters are mounted on each side and measure the distance to the respective measurement cylinders (MC). The tangential deviations $x_1 = s_{\mathrm{s,T}}$ and $x_3 = s_{\mathrm{p,T}}$ can be determined from the data recorded with the distance transmitters and an algorithm presented in Müller et al. (2019). All measurements are carried out with a sampling time of $T_s = 0.001s$.

The tangential deviations $x_1 = s_{\mathrm{s,T}}$ and $x_3 = s_{\mathrm{p,T}}$ are shown in Figure 7 for the speed of $200\,\mathrm{rpm}$ and various
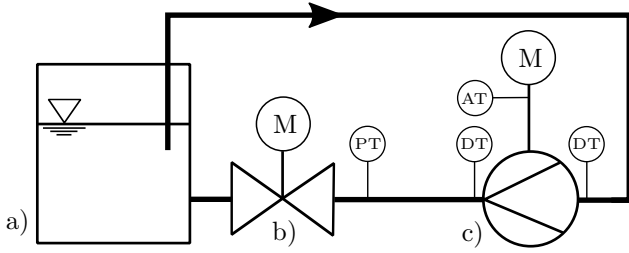
Fig. 5. Test setup including the fluid container a), the control valve b), the PCP c), the pressure transmitter PT, the distance transmitters DT and the angular transmitter AT.
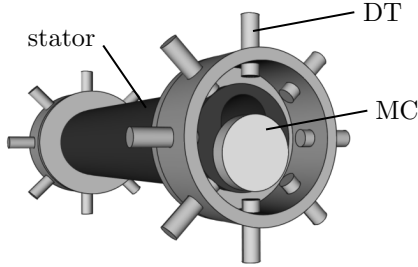


Fig. 6. Rotor and stator combination including mounted measurement cylinder (MC) and sixteen distance transmitters (DT).

differential pressures. The deviations are normalized by dividing them by the maximum deviation $s_{T,max}$. The deviations shown in Figure 7 indicate the suction and pressure side ends of the rotor always move in opposite directions, which corroborates that the rotor carries out a tilting motion. Furthermore, it is evident from Figure 7 that an increased differential pressure results in an increased amplitude of the tilting motion. The angle $\varphi$ is
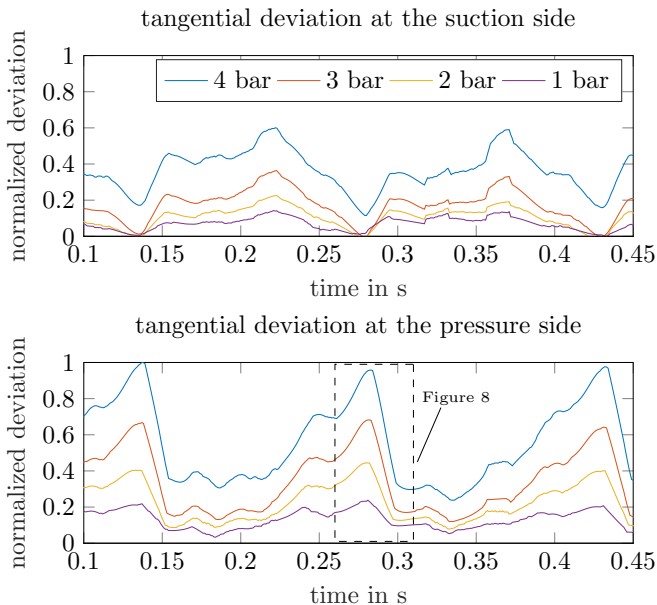


Fig. 7. Tangential deviation of the rotor from its reference path at the suction side and the pressure side for 200 rpm and four differential pressures.

measured with a rotary encoder. The suction and pressure side pressures are measured with pressure sensors.

It remains to determine the angular offset $\gamma(\Delta p)$, which appears in (5). We determine the coefficient $\gamma_1$ of the
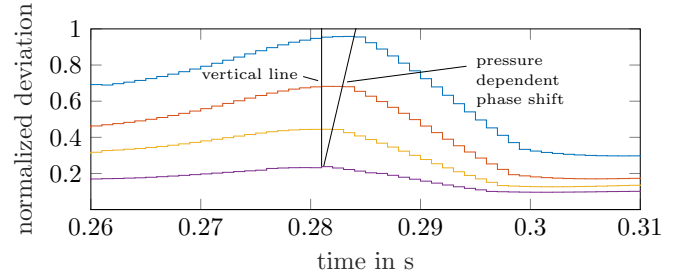


Fig. 8. Pressure dependent phase shift for 200 rpm and four differential pressures.

linear term in (6) with the data shown in Figure 8, which shows the part of Figure 7 that is marked by the dashed rectangle. Note that $\gamma_1$ can be determined reliably despite its small value due to the high sampling rate. After determining $\gamma(\Delta p)$ for an arbitrary but fixed $\Delta p$, the remaining unknown coefficient $\gamma_0$ in (6) can be calculated. It is convenient to determine $\gamma(\Delta p)$ from a polar plot, which is shown for $\Delta p = 4\,\text{bar}$ in Figure 9. We choose $\Delta p = 4\,\text{bar}$, because it results in the largest amplitudes (cf. Figure 7).

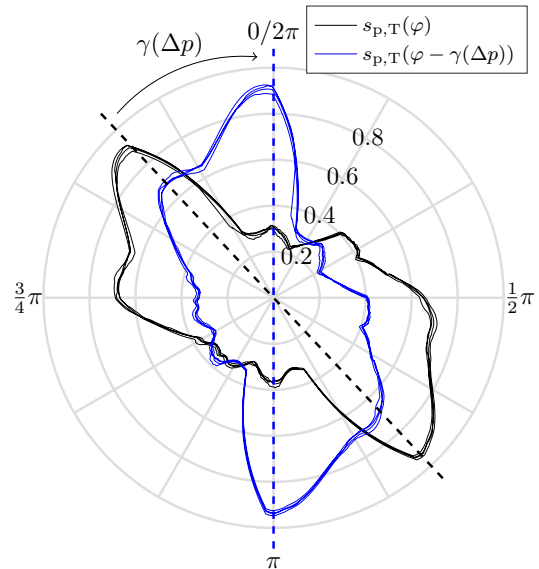We stress again that $\gamma_0$ and $\gamma_1$ only need to be determined once.



Fig. 9. Phase shift between $\varphi$ and $s_{p,T}$ for $\Delta p = 4\,\text{bar}$.

## 4. WEAR DETECTION

The proposed online parameter estimation approach is validated by two distinct experiments. The first experiment examines the convergence of the parameters for the standard size rotor and thus validates the model. The second experiment is performed with an undersize rotor to simulate a worn pump[2].

### 4.1 Parameter estimation for a standard rotor

We apply the model-based parameter estimation method summarized in Section 2 to the test setup sketched in Figure 5. Our studies show that wear can be detected for various pump speeds. Here, the pump speed is arbitrarily

---

[2] All tests are carried out with a Seepex 10-6L single-stage PCP.

chosen to be 200 rpm. The differential pressure is varied in a range from 1 bar to 4 bar. The tangential deviations for these points of operation are shown in Figure 7. The forgetting factor in the RLS algorithm is chosen to be $\lambda = 0.9995$. The initial condition for the parameter vector is set to $\hat{\theta}(0) = [0\ 0\ 0\ 0]^T$. The measurement covariance matrix is set to $P(0) = 10^6 \cdot \mathrm{diag}(1, \ldots, 1)$ to reflect a high uncertainty of $\hat{\theta}(0)$, thus enabling large variations of the parameters in the first few time steps.

All parameter values $c_i$ are normalized by dividing them by the average value of $c_1$ after 1 second of the estimation with 1 bar differential pressure. The values $d_i$ are normalized by dividing them by the average value of $d_1$ after 1 second of the estimation with 1 bar differential pressure.

Figure 10 shows the estimation result for the parameters $c_1$, $c_2$, $d_1$ and $d_2$ for the first 2 seconds for 4 bar differential pressure.
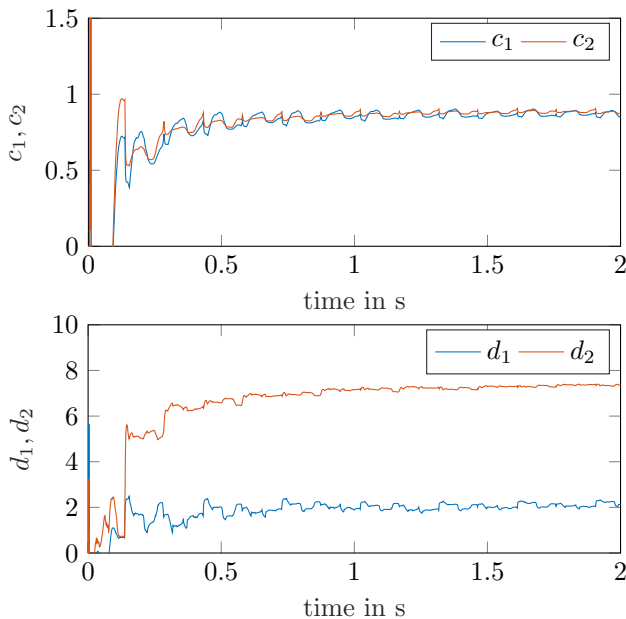


Fig. 10. Convergence of $c_1$, $c_2$ and $d_1$, $d_2$ for 200 rpm and 4 bar differential pressure.

It is evident that all parameters converge to a nearly constant value within about 1 second, which corresponds to $200/60 \approx 3$ rotations of the pump.

Figure 10 demonstrates that the unknown parameters can be estimated with the RLS algorithm and the available measurements. We only discuss the spring constants $c_1$ and $c_2$ in the remainder of the paper and omit the damping constants $d_1$ and $d_2$, because the simulated wear has a more pronounced effect on the spring constants. In fact, we will see further below that monitoring only one of the spring constants, specifically $c_1$, is sufficient to monitor wear.

We briefly analyse the model and its assumption by repeating the online parameter estimation for various differential pressures. Figure 11 shows the online parameter estimation converges for the entire range of differential pressures. The pressure side spring constant $c_2$ converges to values that vary only weakly with the differential pressure (3.7 %). The suction side spring constant $c_1$, however, varies within 13.4 %.

This indicates the linear spring models in (1)-(4) only approximate the system behaviour and must be replaced by nonlinear springs if the amplitudes of $s_{\mathrm{p,T}}$ and $s_{\mathrm{s,T}}$ get too large. Nevertheless, we claim that the model (1)-(4) is sufficiently precise for its intended use for wear detection. This will be evident from the comparison of the experimental results discussed so far to those for an undersize rotor in the subsequent section.
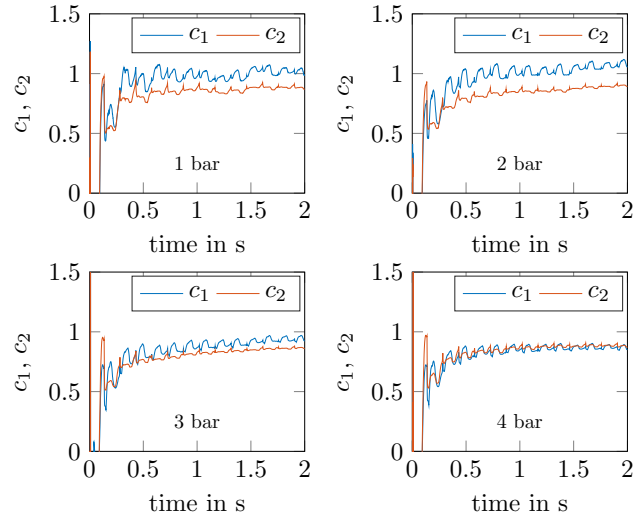


Fig. 11. Convergence of $c_1$ and $c_2$ for 200 rpm and various differential pressures.

### 4.2 Comparison to results for an undersize rotor

Wear essentially results in the rotor and stator to shrink due to material abrasion (Sathyamoorthy et al., 2013). We use an undersize rotor to simulate this effect. The radius of the rotor $r_R$ was reduced by approximately 0.92 %. This reduction of $r_R$ still leads to a tight contact between the rotor and the stator. Figure 12 shows a sketch of the contact areas for both radii, the standard size rotor radius $r_R$ and the radius of the undersize rotor $r_{R,u}$.
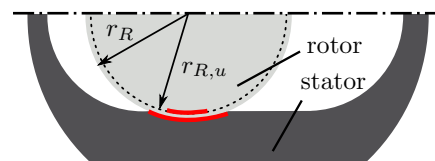


Fig. 12. Overlap between rotor and stator. The red lines mark contact areas for the standard and the undersize rotor.

The spring constants in (1)-(4) depend on the contact area between rotor and stator, depicted by the red lines in Figure 12. As the area of the contact zone becomes smaller with the undersize rotor, less stator material contributes to the repulsive forces modeled with the spring constants $c_i$. We therefore expect a larger amplitude of the rotor tilting and lower values for the spring constants $c_i$ for the undersize rotor.

We apply the same estimation procedure as in Section 4.1 to the measurements carried out with the undersize rotor. The estimation again is performed for 200 rpm and differential pressures ranging from 1 bar to 4 bar. Figure 13 compares the estimation results obtained with the undersize rotor to those for the standard rotor. First note

that the estimation procedure converges in all cases. More importantly, the data show significantly different values for the spring constant $c_1$ for the standard ($c_{1,s}$) and the undersize rotor ($c_{1,u}$).

For 4 bar, which is the point of operation for which $c_{1,s}$ and $c_{1,u}$ are closest to each other, they converge to average values that differ by 47.4 %. This value is significantly larger than the largest standard deviation (6.35 %) and significantly larger than the variation of $c_1$ with the differential pressures shown in Figure 11. This indicates that the wear simulated with the undersize rotor can easily be detected and $c_1$ can serve as an indicator for wear.

The most significant difference results for $c_1$. We show the comparison of $c_{2,s}$ and $c_{2,u}$ for completeness only (see Figure 14).
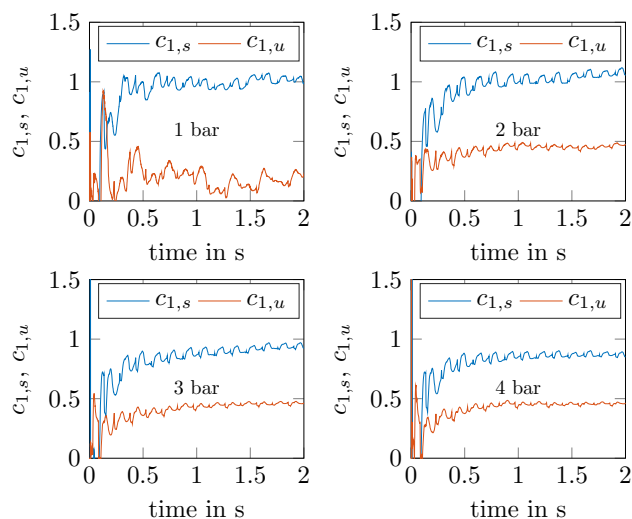


Fig. 13. Comparison between the estimation for the standard ($c_{1,s}$) and the undersize rotor ($c_{1,u}$) for 200 rpm and various differential pressures.
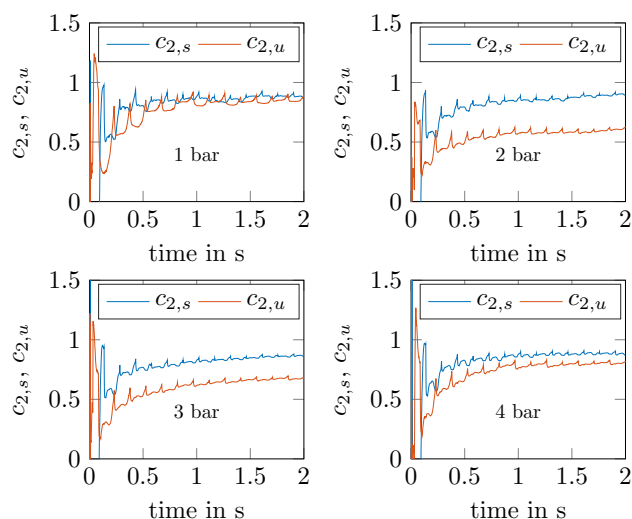


Fig. 14. Comparison between the estimation for the standard ($c_{2,s}$) and the undersize rotor ($c_{2,u}$) for 200 rpm and various differential pressures.

## 5. CONCLUSION AND OUTLOOK

Our results show that the proposed online parameter estimation can be used to monitor the wear of progressing

cavity pumps. Specifically, the online estimation of the suction side spring constant $c_1$ proved to be appropriate for this purpose. We showed even very small changes in the rotor radius (less than 1% here) lead to significant changes in the estimated parameter $c_1$, which implies $c_1$ is suitable for an online wear detection.

The parameter estimation is based on a simple model (1)-(4), which (after $\gamma(\Delta p)$ is determined once) only depends on design parameters accessible by data sheets and on parameters that can automatically be determined with the proposed estimation procedure. Consequently, the proposed method can be applied to a wide range of industrial progressing cavity pumps.

The presented approach requires only simple online calculations and therefore can be implemented on embedded hardware.

Further research will focus on reducing the number of sensors and on modeling the remaining service life of the pump as a function of $c_1$.

REFERENCES

Åström, K.J. and Wittenmark, B. (1989). *Adaptive Control.* Addison-Wesley Publishing Company, first edition.

Delpassand, M. (1997). Progressing cavity (PC) pump design optimization for abrasive applications. In *Proceedings of the SPE Production Operations Sympsiom*, 1–5.

Liang, Y., Cao, G., Shi, G., Wang, G., Li, J., and Zhao, Y. (2011). Progressing cavity pump anti-scaling techniques in alkaline-surfactant-polymer flooding in the Daqing Oilfield. *Petroleum Exploration and Development*, 38(4), 483–490.

Mohanty, A., Pradhan, P., Mahalik, N., and Ghosh Dastidar, S. (2012). Fault detection in a centrifugal pump using vibration and motor current signature analysis. *Int. J. of Automation and Control*, 6, 261–276.

Müller, J., Leonow, S., Schulz, J., Hansen, C., and Mönnigmann, M. (2019). Towards model-based condition monitoring for progressing cavity pumps. In *Proceedings of the 4th International Rotating Equipment Conference*, 1–10.

Müller, M. (2017). *Evaluation of the rotor position in a progressive cavity pump under varying operational parameters (in German).* Master's thesis, Ruhr-Universität Bochum.

Nelik, L. and Brennan, J. (2005). *Gulf Pump Guides: Progressing Cavity Pumps, Downhole Pumps and Mudmotors.* Gulf Publishing Company.

Nguyen, N.T. (2018). *Model-Reference Adaptive Control.* Advanced Textbooks in Control and Signal Processing. Springer.

Sathyamoorthy, S., Steyn, A., McGilvray, J., Fuchs, H., Ainebyona, B., Kyomugisha, P., Vijapurapu, S., Kagga, N., Rindfuss, R., and Basiima, D. (2013). First Application of Progressing Cavity Pumps for Appraisal Well Testing in the Ugandan Albertine Graben Basin. *SPE Production & Operations*, 28(1), 85–94.

Wirth, W. (1993). *On the hydraulic and tribological modeling of progressing cavity pumps (in German).* Ph.D. thesis, Universität Erlangen-Nürnberg.